# Comparison and Synergy of BPSK and BOC Modulations in GNSS Reflectometry

Jyh-Ching Juang, *Member, IEEE*, Chen-Tsung Lin, and Yung-Fu Tsai

***Abstract*—Signals from global navigation satellite systems (GNSSs) have been advocated as opportunities for remote sensing of the Earth. In the multi-GNSS era, signals from different constellation, at different frequency, and under different modulation are available to facilitate such applications. Existing open service GNSS signals can be roughly categorized as either binary phase-shift keying (BPSK) modulation or binary offset carrier (BOC) modulation; it is desired to establish a unified data processing procedure to account for all these signals. This article proposes a framework to synergize BPSK and BOC signals for GNSS reflectometry (GNSS-R) applications by establishing a channel response function to model the scattering phenomena and a commutative diagram to illustrate the interrelationship among direct and reflected signals under different modulations. The results are verified by processing the flight test data of the GNSS-R receiver of the TRITON mission.**

***Index Terms*—Binary offset carrier (BOC), binary phase-shift keying (BPSK), channel response function, global navigation satellite system (GNSS), reflectometry, TRITON.**

## I. Introduction

GLOBAL navigation satellite systems (GNSSs), including USA's Global Positioning System (GPS) [1], Russia's GLObal NAvigation Satellite System [2], European Union's Galileo [3], China's Beidou [4], Japan's Quasi-Zenith Satellite System (QZSS) [5], and so forth, provide highly accurate and reliable signals for positioning, navigation, and timing (PNT) service. In the remote sensing community, the same signals have also been exploited through radio occultation and reflectometry techniques to retrieve information about the atmosphere and surface of the Earth [6]–[8]. The GNSS reflectometry (GNSS-R) remote sensing operates in a multistatic radar principle, in which the orbiting GNSS satellites transmit high-quality signals and the receiver processes the reflected GNSS signals from the surface of the Earth so that properties such as ocean wind, ice layer thickness, and soil moisture can be retrieved. Some pioneering works on GNSS-R can be found in [9]–[11], among many others. For spaceborne missions, the reception of reflected GPS signals is reported in [12]. Ever since, several space missions notably U.K. Disaster Monitoring Constellation [13], [14] and TechDemoSat-1 (TDS-1) [15], [16] have been conducted to verify the feasibility of using GPS reflected signals for sea state determination and ice monitoring. More recently, NASA Cyclone Global Navigation Satellite System (CYGNSS) mission has utilized eight satellites to measure wind speeds over Earth's oceans with the scientific goal of understanding and predicting hurricanes [17]–[19]. The National Space Organization (NSPO), Taiwan, is conducting the TRITON or FORMOSAT-7R program, which is a space-based GNSS-R mission to perform remote sensing of the ocean surface roughness and wind speed in an attempt to provide crucial data for severe weather research and prediction [20], [21]. The TRITON is named after a god of the sea in Greek mythology.

Existing missions, including TDS-1 and CYGNSS, primarily process reflected signals from GPS satellites. In the multi-GNSS era, several GNSS signal components at different frequencies and under different modulations can be employed for remote sensing applications. A technical objective of the TRITON mission is to exploit the opportunities of multi-GNSS signals for reflectometry study. To this end, the TRITON GNSS-R receiver is designed to process GPS, Galileo, and QZSS signals. Unlike GPS legacy signals that are modulated through a binary phase-shift keying (BPSK) scheme, recent open service GNSS signals such as those from Galileo and GPS III satellites adopt some variations of the binary offset carrier (BOC) modulation to achieve spectral efficiency, compatibility, and interoperability [22]–[24]. A BOC-modulated signal can be obtained by multiplying a BPSK signal with a square-wave-type subcarrier. This extra subcarrier alters the shape of the autocorrelation function, making the main peak narrower. In PNT application, BOC modulation results in a higher tracking accuracy and a better multipath mitigation capability at the expense of processing complexity. It is expected that the presence of BOC-modulated signals will be beneficial in GNSS-R applications in terms of quantity and quality. Indeed, the increase of the satellites and signal components enhances the spatial/temporal coverage and opportunities of remote sensing. It is also expected that the narrow peak of the autocorrelation function yields a better spatial resolution. In [25], waveforms of reflected GPS and Galileo signals under bandwidth limitation are simulated, and the benefit of BOC modulation in providing a higher precision altimetry application is discussed.

Given that GPS and Galileo signals are available for reflectometry applications, it is desired to process both BPSK- and

Manuscript received December 30, 2019; revised March 15, 2020 and April 7, 2020; accepted April 16, 2020. Date of publication April 30, 2020; date of current version May 21, 2020. This work was supported in part by the Ministry of Science and Technology, Taiwan, under Grant MOST 108-2218-E-006-022 and in part by the National Space Organization, Taiwan, under Grant NSPO-S-107151. *(Corresponding author: Jyh-Ching Juang.)*

Jyh-Ching Juang is with the Department of Electrical Engineering, National Cheng Kung University, Tainan 70101, Taiwan (e-mail: juang@mail.ncku.edu.tw).

Chen-Tsung Lin and Yung-Fu Tsai are with the National Space Organization, Hsinchu 30078, Taiwan (e-mail: tomlin@nspo.narl.org.tw; raymond@narlabs.org.tw).

Digital Object Identifier 10.1109/JSTARS.2020.2989824

BOC-modulated signals in the same data processing chain. One contribution of this article is to develop a channel response function to relate the measured waveforms of the direct line-of-sight (LOS) signal and the reflected signal. It is shown that the channel response function is applicable to both BPSK and BOC signals. As a result, even though the waveforms or squared autocorrelation functions of BPSK and BOC signals are different, the data processing and retrieval tasks can be conducted under the same framework.

In existing GNSS-R data retrieval approaches, the delay Doppler map (DDM) or waveform measurement of the reflected signals and the knowledge of the transmitted power of the GNSS satellite are evaluated against the scattering model [11], [26] to estimate the remote sensing parameters such as the ocean wind speed. Hence, the results depend on the transmitted power of the GNSS satellite, which may be subject to variations. A benefit of the proposed channel response function is that it is not sensitive to the change of the transmitted power, since the measured direct LOS signal and reflected signal are equally affected. A lesson learned in the CYGNSS mission is that the calibration of the instrument and validation of the data [27], [28] are challenging even though the use of an intercalibration technique [29] has been investigated. The relaxation on the knowledge of the transmitted power of the proposed framework has an implication on the calibration of the GNSS-R receiver.

Each GPS III and QZSS satellite broadcasts both BPSK- and BOC-modulated signals at the same time. A GNSS-R receiver can thus receive two signals with different modulations along the same reflection path. Based on the aforementioned framework, a synergy scheme for BPSK- and BOC-modulated signals in reflectometry is proposed. To this end, the BOC signal waveform is expressed as a function of the BPSK signal waveform, and through the aforementioned channel response function, a commutative diagram is established so that the signal quality and retrieved result can be monitored and assessed.

The remainder of this article is organized as follows. In Section II, the TRITON mission is described, and the requirements and configurations of the GNSS-R receiver payload are discussed. In Section III, signal processing of GNSS-R is discussed. It is shown that the adjustment of the open-loop tracking parameters demands special consideration to account for the dynamics of a spaceborne receiver and the variation in a scattering environment. Some design considerations are discussed, and the implementation in the TRITON GNSS-R receiver is presented. In Section IV, the channel response function is developed to model the relationship between the direct LOS signal waveform and the scattered signal waveform. This modeling approach provides a characterization of the scattering phenomena and paves the way for data retrieval. Based on the channel response function, a synergy scheme of BPSK- and BOC-modulated signals is established by using a commutative diagram. In Section V, test data are processed to compare BPSK- and BOC-modulated signals and to verify the channel response function model. In addition, the synergy is assessed by processing reflected QZSS signals. Finally, Section VI concludes this article.

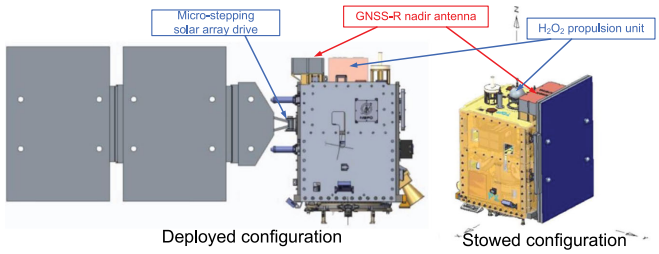


Fig. 1. TRITON satellite configuration.

## II. TRITON Mission

In this section, the TRITON mission, satellite, and the GNSS-R receiver payload are briefly described.

### A. Mission

The TRITON mission is a technology demonstration mission to fulfill two objectives: satellite bus technology demonstration and GNSS-R remote sensing assessment. For the former, some key satellite bus technologies, including optimized on-board computer and power control unit, $H_2O_2$ propulsion subsystem, attitude control components and algorithms, and microstepping solar array driving module, are designed and supplied from domestic industries in an attempt to increase the technology readiness level through on-orbit tests. For the latter, a spaceborne GNSS-R receiver payload and a data processing system are developed to measure ocean scattered signals for ocean wind retrieval so as to pave a way for severe weather research. The TRITON GNSS-R receiver is an indigenous design with the vision that GNSS-R measurements can complement NSPO FORMOSAT-7 radio occultation mission [30] in the data assimilation process for the enhancement of the prediction capability of the intensity and track of typhoons. The execution of the TRITON mission is thus influenced by the NASA CYGNSS mission as both share a similar objective in utilizing the GNSS-R technique to retrieve wind information for severe weather research. There are, nevertheless, some discrepancies in terms of satellite design, orbit, data retrieval, assimilation model, and payload design, as will be discussed in the following.

The configuration of the 300-kg class TRITON satellite is depicted in Fig. 1. In the stowed configuration, the dimension is approximately $100 \times 120 \times 125$ cm$^3$. The GNSS-R receiver antenna is on the top panel in the figure, which will be in the nadir direction when the satellite is in orbit. The figure also highlights two design features of the satellite bus, namely, $H_2O_2$ propulsion unit and microstepping solar array driving module. Two solar panels are deployed when in orbit to provide a sufficient level of power for the operation. The TRITON is a Sun-synchronous orbit satellite at 550-km altitude. The pointing accuracy is required to be better than $0.1^\circ$ so that the pointing location of the main beam of the reception antenna can be georeferenced to about 1 km. The satellite is expected to be launched in 2021.

### B. TRITON GNSS-R Payload

The TRITON GNSS-R payload receives and processes both the direct LOS and reflected GNSS signals so that features on the

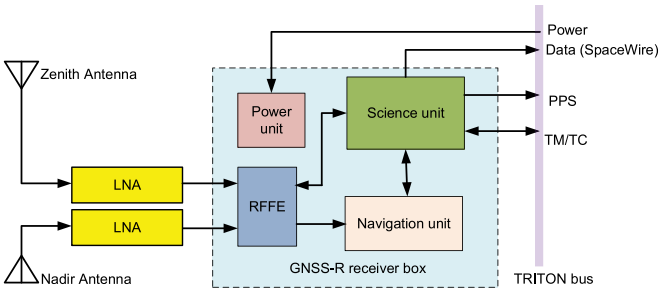


Fig. 2. Block diagram of the TRITON GNSS-R receiver.

surface of the earth can be retrieved. In particular, the retrieval of the wind speed over the ocean is deemed as an important task of the program. The GNSS-R receiver is indeed a scatterometer, and the design requirements are as follows [20].

1) The GNSS-R receiver shall be able to process reflected GPS L1 signals and generate the associated DDM either autonomously or by schedule.
2) The size of the DDM shall be at least 128 (in code phase) $\times$ 64 (in frequency bin), and each entry of the DDM shall be at least 16 bits.
3) The GNSS-R receiver shall be capable of processing four DDMs simultaneously.
4) The DDM update rate shall be at least 1 s.
5) The GNSS-R receiver shall be able to record direct LOS and reflected GPS, QZSS, and Galileo signals in L1 and L2 bands in raw data format at the intermediate frequency (IF) for ground postprocessing purpose.
6) The GNSS-R receiver shall be designed with a process-and-record model for ground debugging purpose.
7) The GNSS-R receiver shall facilitate metadata to support calibration and retrieval.
8) The GNSS-R receiver shall potentially be extended to process reflected QZSS and Galileo signals and generate DDMs of the aforementioned space, magnitude, and time resolution in real time.

The TRITON GNSS-R receiver contains antennas, low-noise amplifiers (LNAs), radio frequency front ends (RFFEs), navigation unit, and science unit. As shown in the block diagram of Fig. 2, the RFFEs, navigation unit, and science unit are installed in the receiver box. The zenith antenna is a dual-frequency (L1+L2) right-hand circularly polarized antenna that is used to receive direct LOS GNSS signals. In contrast, the nadir antenna is a dual-frequency left-hand circularly polarized antenna with eight elements that is used to receive reflected signals. The LNAs are employed to increase the signal power with an acceptable noise figure, and the RFFEs are responsible for signal amplification, filtering, signal conditioning, downconversion, and analog-to-digital conversion. The RFFE samples the incoming signals at a rate of $16.368 \times 10^6$ samples/s. Each sample is represented as a 4-bit complex data, which are processed in real time to generate the DDM or archived for data downlink and postprocessing. The navigation unit provides position, velocity, and timing information as well as tracking information based on the received signals at the zenith antenna. The timing information is to synchronize the operation of the DDM generation. The position information together with the orbit information of the GNSS satellite is used in the reflection management routine to compute the specular reflection point. Moreover, the tracking information such as code phase, code phase rate, and Doppler frequency is used to in motion compensation routine to determine the arguments of the DDM. The science unit is the kernel of the GNSS-R receiver. In addition to performing the aforementioned synchronization, management, and allocation tasks, the science unit is also responsible for the generation of the DDM in real time. To this end, a conventional GNSS-R technology is adopted, in which a set of local code and Doppler frequency replica is generated to correlate with the incoming signals. The correlation processing is a combination of coherent integration and noncoherent accumulation. The coherent integration is accomplished by using a fast Fourier transform approach and implemented in a field-programmable gate array. The noncoherent accumulation is realized by using an embedded processor. At each coherent integration period, the reference code phase and Doppler frequency are adjusted to reflect the dynamics of the observation geometry. The operation of the science unit is governed by a state machine, and the TRITON satellite can send command to change the operating mode, and in the meantime, the status of the receiver is sent to the satellite bus. Details on the GNSS-R signal processing are discussed in the next section.

## III. GNSS-R Signal Processing

A GNSS-R receiver typically employs a set of correlators to carry out long-integration tasks and form the DDM. The retrieved data associated with the reflecting surface from the DDM thus depend on the design of the correlation schemes. In this section, the effects of correlation processing are analyzed for both BPSK- and BOC-modulated signals. The design features of the TRITON GNSS-R receiver are then discussed.

### A. BPSK and BOC Signal Processing

The GNSS signal under consideration can be expressed as

$$u(t) = \sqrt{2P_c} \cdot d(t) \cdot g(t) \cdot s(t) \cdot \cos(2\pi f_L t) \qquad (1)$$

where $P_c$ is the power of the signal, $d(t)$ is the navigation data, $g(t)$ is the spreading code, $s(t)$ is the subcarrier, and $f_L$ is the carrier frequency. The above model can be used to characterize BPSK- and BOC-modulated GNSS signals. The BOC-modulated signals differ from BPSK-modulated signals by the subcarrier $s(t)$. In the case of BPSK modulation, the subcarrier $s(t) = 1$ is a constant. In contrast, if a sine-phased BOC modulation is used, $s(t) = \text{sgn}(\sin(2\pi f_{\text{sc}} t))$ , where sgn is the sign function and $f_{\text{sc}}$ is the subcarrier frequency. It is noted that the sign function of $\cos(2\pi f_{\text{sc}} t)$ is used in some GNSS signal components. In practice, the exact implementation in GPS III and Galileo is the multiplexed BOC (MBOC) modulation [22], [23]. Thus, one should compare BPSK with MBOC when considering actual GPS versus Galileo signals or GPS II versus GPS III signals. However, as MBOC and BOC signals

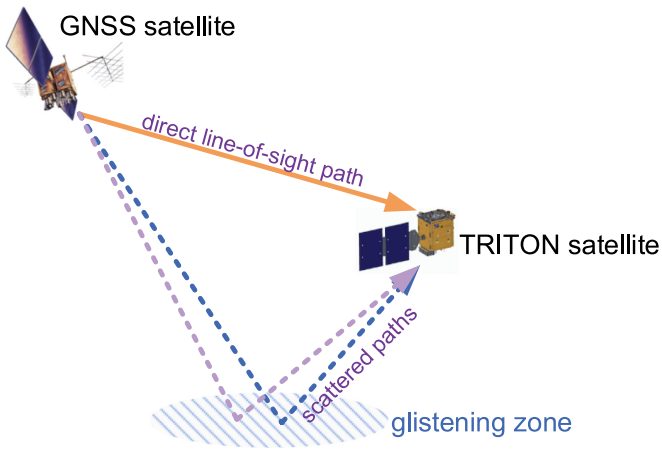


Fig. 3. Direct LOS and scattered signal paths.

are similar in characteristics especially when the bandwidth is limited, we will thus discuss the BPSK(1)- and sine-phased BOC(1,1)-modulated signals in the following sections. Here, BPSK(1) is the BPSK signal with chip rate $f_c$ of the spreading code being 1.023 Mcps (megachips per second) and BOC(1,1) refers to the BOC-modulated signal in which the chip rate is 1.023 Mcps and the subcarrier frequency is 1.023 MHz.

Along the transmission path from the GNSS satellite to the receiver, the GNSS signals are subject to fading, delay, Doppler shift, atmospheric effect, noise, and possibly interference. The effects are more pronounced and further aggravated by surface-induced phenomena for scattered signals as both specular and diffuse reflections may coexist. As a result, the received signal can be considered as a distributed summation of attenuated, shifted, and distorted versions of the transmitted signal, which is then contaminated with noise. In the receiver, as described previously, the signal is amplified, filtered, downconverted, and digitized at the RFFE. This then results in a sequence of digital IF samples in Eqn. (2), shown at the bottom of this page. where $j=\sqrt{-1}$, $n$ stands for sampling epoch, $T_s$ is the sampling interval, which is related to the sampling frequency $f_s$ through $T_s=1/f_s$, and $w[n]$ is the noise. In (2), the signal along the $i$th propagation path is characterized by its signal power $P_i$, propagation delay $\tau_i$, Doppler frequency $f_{D,i}$, and phase $\phi_i$. Each path may come from the GNSS satellite to a point on the glistening zone and then to the GNSS-R receiver, as depicted in Fig. 3. The variable $m_i$ represents the contribution of the $i$th scattered component on the received signal $r[n]$. In the extreme case when only the specular reflected component is considered, the number of path becomes one and the corresponding $m_i$ is 1.

In general, the glistening zone is decomposed into cells, the path can be considered as from each cell, and the variable $m_i$ is related to the bistatic radar cross section, which is related to the probability density function of the mean squared slope of the cell. It is remarked that the signal $r[n]$ may be subject to front-end filtering effect, and as a result, the data, spreading code, and subcarrier need to be replaced with the equivalent filtered versions. The noise term can indeed contain effect due to cross correlation [23]. Hereafter, for simplicity, the noise term $w[n]$ is assumed to be a zero-mean white Gaussian sequence with variance $\sigma^2$, which depends on the noise temperature at the antenna and bandwidth of the front end filter. Also, the presence of navigation data is neglected afterward. This simplification is justifiable as the coherent integration time is much shorter than the navigation data period. Even though a data transition within the coherent integration time may result in correlation loss, the effect typically becomes insignificant after a squaring operation in noncoherent accumulation. It is remarked that in the GNSS-R receiver, it is possible to decode the navigation data from the direct LOS signals and aid the processing of reflected signals. Furthermore, the navigation data issue can be relaxed if one chooses to process the pilot (dataless) signal components such as Galileo E1C signals.

In the GNSS-R receiver, the GNSS-R observable DDM is obtained by correlating the incoming signal with a set of locally generated replicas at different code phase delay estimates and Doppler frequency estimates. The DDM is a $P\times Q$ array, where $P$ is the number of code phase delays and $Q$ is the number of Doppler frequencies under consideration. Let $\hat{\tau}_p$ with $1\le p\le P$ and $\hat{f}_{D,q}$, with $1\le q\le Q$ be the code phase delay and Doppler frequency estimates, respectively. The corresponding local replica can be expressed as

$$r_{p,q}[n]=g(nT_s-\hat{\tau}_p)\cdot s(nT_s-\hat{\tau}_p)\cdot\exp(-j2\pi(f_{\text{IF}}+\hat{f}_{D,q})nT_s). \tag{3}$$

Each element of the DDM is obtained by performing coherent processing, squaring operation, and noncoherent accumulation to enhance the signal-to-noise ratio and to relax the sensitivity on signal coherence and navigation data transition. The coherent processing is to perform the following operation:

$$z_{p,q}[k]=\frac{1}{N}\sum_{n=kN}^{kN+N-1} r[n]\cdot r_{p,q}[n] \tag{4}$$

where $N$ is the number of samples that are multiplied and accumulated in the coherent processing. In general, $N$ is selected so that the coherent integration time $T_{\text{coh}}=NT_s$ is an integer multiple of the period of the spreading code. Substituting (2)

$$r[n]=\sum_i m_i\sqrt{P_i}\cdot d(nT_s-\tau_i)\cdot g(nT_s-\tau_i)\cdot s(nT_s-\tau_i)\cdot\exp(j2\pi(f_{\text{IF}}+f_{D,i})nT_s+\phi_i)+w[n] \tag{2}$$

$$\chi(\tau_i,\hat{\tau}_p,f_{D,i},\hat{f}_{D,q},k)=\frac{1}{N}\sum_{n=kN}^{kN+N-1} g(nT_s-\tau_i)\cdot g(nT_s-\hat{\tau}_p)\cdot s(nT_s-\tau_i)\cdot s(nT_s-\hat{\tau}_p)\cdot\exp(j2\pi(f_{D,i}-\hat{f}_{D,q})nT_s) \tag{6}$$

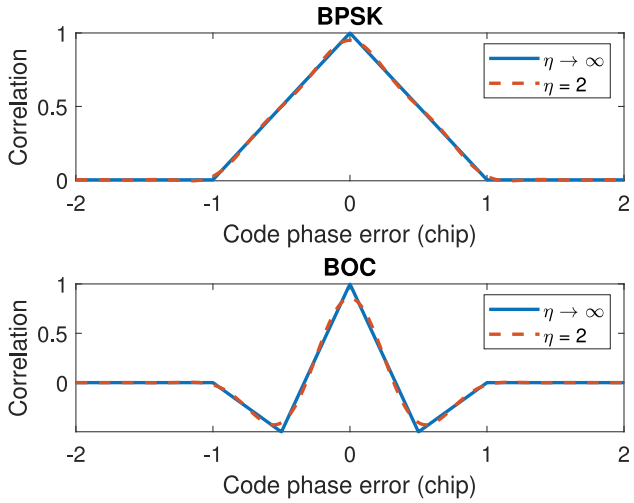


Fig. 4. Normalized autocorrelation functions.

and (3) into (4) results in

$$z_{p,q}[k] = \sum_i m_i \sqrt{P_i} \cdot \chi(\tau_i, \hat{\tau}_p, f_{D,i}, \hat{f}_{D,q}, k) \cdot \exp(j2\pi\phi_i) + v_{p,q}[k] \tag{5}$$

where the function $\chi(\tau_i, \hat{\tau}_p, f_{D,i}, \hat{f}_{D,q}, k)$ is defined in (6) shown at the bottom of previous page, and $v_{p,q}[k]$ is the noise term. The function $\chi(\tau_i, \hat{\tau}_p, f_{D,i}, \hat{f}_{D,q}, k)$, which is referred to as the generalized correlation function or Woodward ambiguity function, plays an important role in the GNSS-R signal processing and data retrieval. The function can be approximated as a product of a code-phase-error-dependent autocorrelation function and a Doppler-frequency-error-dependent function [26] as

$$\chi(\tau_i, \hat{\tau}_p, f_{D,i}, \hat{f}_{D,q}, k) \approx \Lambda(\tau_i - \hat{\tau}_p) \cdot \mathrm{sinc}((f_{D,i} - \hat{f}_{D,q})NT_s) \tag{7}$$

where $\Lambda$ is the autocorrelation function and the sinc function is defined as $\mathrm{sinc}(x) = \frac{\sin(\pi x)}{\pi x}$. The two functions are locally supported, i.e., the $i$th scattered signal can be observed only when both $|\tau_i - \hat{\tau}_p|$ and $|f_{D,i} - \hat{f}_{D,q}|$ are small. Indeed, the main lobe of the sinc function is for the Doppler frequency error $f_{D,i} - \hat{f}_{D,q}$ to be bounded by $-\frac{1}{T_{\text{coh}}}$ and $\frac{1}{T_{\text{coh}}}$. Let $T_c$ be the chip interval; the autocorrelation function becomes zero when $|\tau_i - \hat{\tau}_p| > T_c$. The shape of the autocorrelation function depends on the modulation and the bandwidth. Let $B$ be the bandwidth and define the bandwidth factor $\eta = BT_c$; the autocorrelation functions of the BPSK- and BOC-modulated signals for $\eta \to \infty$ and $\eta = 2$ cases are depicted in Fig. 4. The autocorrelation function of the BPSK-modulated signals is of the triangular shape. In contrast, the BOC-modulated signals render an autocorrelation function that has a peak with two accompanying troughs. It is noted that the main lobe becomes narrower in comparison with its BPSK counterpart, implying a better ranging accuracy and multipath mitigation. In the band-limited cases, the autocorrelation functions are no longer piecewise linear, and a correlation loss is observed. When $\eta = 2$, the losses are 0.45 and 1.35 dB for BPSK- and BOC-modulated signals, respectively.

After the coherent processing, the complex $z_{p,q}[k]$ is squared to remove the dependence on the phase $\phi_i$ and the navigation data. The squared terms are then accumulated noncoherently to further enhance the signal-to-noise ratio. The noncoherent accumulation is realized through

$$y_{p,q} = \frac{1}{K} \sum_{k=0}^{K-1} |z_{p,q}[k]|^2 \tag{8}$$

where $K$ is the number of accumulations. This accumulation can further enhance the signal-to-noise ratio by a factor $10 \log_{10} K$ at the expense of squaring loss. The noncoherent accumulation result $y_{p,q}$ is the DDM observable with the code phase estimate $\hat{\tau}_p$ and the Doppler frequency estimate $\hat{f}_{D,q}$. The integration time to generate a DDM is thus $T_{\text{int}} = K \cdot T_{\text{coh}} = K \cdot N \cdot T_s$.

### *B. Design Features in TRITON GNSS-R Signal Processing*

To generate the DDM in (8), it is imperative to determine the input variables: code phase estimate $\hat{\tau}_p$, Doppler frequency estimate $\hat{f}_{D,q}$, coherent integration interval $N$, noncoherent accumulation interval $K$, number of code phases $P$, and number of Doppler bins $Q$. The latter two numbers $P$ and $Q$ are set based on requirement 2) discussed in Section II-B. The overall integration time $T_{\text{int}}$ is 1 s according to requirement 4), which constrains the product $K \cdot N$, as $T_s$ is the reciprocal of the sampling rate. The coherent integration interval $N$ in samples is determined by assessing the coherence time, GNSS signal characteristics, and orbit dynamics. For scattered signals, the phase coherence depends on the observation geometry, relative velocity and surface properties (see [31]). Based on a formula on the analysis of the coherence time [12], it is found that for the TRITON GNSS-R receiver, which is planned to be operating at 550-km altitude, the coherence time with respect to chipping rate of 1.023 Mcps is about 1.3 ms when the reflection event occurs at the nadir direction. The coherence time may become shorter in high-wind and rough-sea situations. The spreading code periods of the GPS L1 C/A, Galileo E1, and GPS/QZSS L1C signals are 1, 4, and 10 ms, respectively. Thus, a coherent processing for a full spreading code period for BOC-modulated E1 and L1C signals may result in a correlation loss. This issue can be accounted for by using the partial correlation or double-block zero padding technique [32], [33]. After examining the implementation complexity, the coherent integration time is maintained as the same as the period of the spreading code. Therefore, to process GPS L1 C/A signals, the variables are set as $N = 16\,368$ and $K = 1000$. The variables become $N = 65\,472$ and $K = 250$ for Galileo E1 signals.

The variables $\hat{\tau}_p$ and $\hat{f}_{D,q}$ need to be adjusted by examining the relative geometry between the TRITON and the GNSS satellite. To this end, both the positions of the TRITON and GNSS satellite are obtained from the navigation unit. Consequently, the specular reflection point is estimated based on a quasi-spherical Earth approach [34], and the code phase delay $\hat{\tau}_p$ is computed. Likewise, the Doppler frequency $\hat{f}_{D,q}$ is also

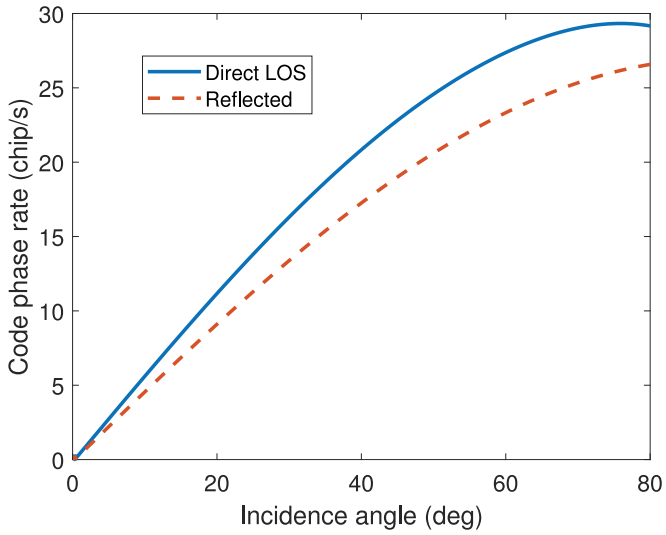


Fig. 5. Code phase rate.

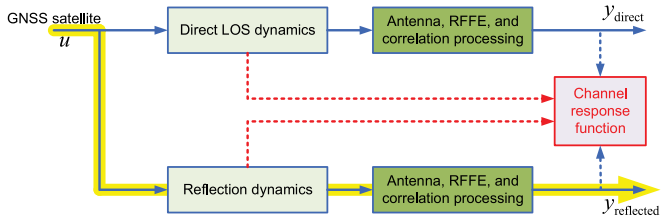


Fig. 6. Channel response function is used to relate the propagation dynamics.

estimated based on the relative velocities of the TRITON and the GNSS satellite. Two issues that need to be addressed are the rate of the code phase and the deviation of the chip interval. The relative velocity between the GNSS satellite and the GNSS-R receiver for either the direct LOS path or the reflection path is significant. The code phase rate for a satellite at 550 km with respect to a GPS satellite in terms of L1 C/A code chip as a function of the incidence angle is depicted in Fig. 5. Note that at an incidence angle of 20°, the code phase rate reaches 9.18 chips/s for a reflected signal. The code phase rate is even faster for the direct LOS signal. For a GNSS-R receiver, this implies that the code phase estimate $\hat{\tau}_p$ must be adjusted accordingly. In the TRITON GNSS-R receiver, this adjustment is accomplished by combining the code rate tracking of the LOS signal from the navigation unit [35] and a correction term from a lookup table that delineates the code phase rate difference between the direct LOS and reflected signals as a function of the incidence angle. The code phase variable at the next epoch is thus determined by the current code phase estimate and the code phase rate estimate. In the presence of Doppler frequency shift, the chip interval deviates from its nominal value. The actual chip expands or shrinks as a function of the Doppler frequency according to

$$T_c^{'} = T_c \frac{f_L}{f_L + f_D}. \tag{9}$$

This essentially implies that after $|\frac{f_L+f_D}{f_D}|$ chip intervals, the local replica and the incoming signal are offset by one chip, making them uncorrelated. As an example, if the Doppler frequency is 8 kHz, then the local replica and incoming signal becomes uncorrelated after 192.5 ms for the GPS L1 C/A signal component. For the BOC-modulated signal, the loss of correlation is more pronounced. Before the complete loss of correlation, in which the local symbol deviates from the incoming signal by one symbol, a correlation loss can be expected. Thus, if the power at the peak of the DDM is used for data retrieval, this correlation loss needs to be accounted for. Unfortunately, a long integration is deemed essential from the link budget perspective in GNSS-R application especially when the antenna gain is low. Therefore, the design needs to achieve a balance between implementation complexity and correlation loss. To this end, the coherent processing interval is limited to 1 ms in the TRITON GNSS-R receiver, and the code phase and Doppler frequency estimates are appropriately adjusted between consecutive noncoherent accumulations. The above features have been implemented in the science unit of the GNSS-R receiver.

## IV. Channel Response Function for the Synergy of BPSK/BOC Signals

The TRITON GNSS-R payload is equipped with zenith and nadir antennas to receive the direct LOS and reflected signals, respectively. With respect to an orbiting GNSS satellite, the receiver can thus perform correlation operation to yield DDMs or delay waveforms along the two paths, which are illustrated in Fig. 3. In this section, the channel response function is proposed to characterize the difference between the two waveforms. Under the channel-response-function-based framework, a method for data synergy is then investigated.

### A. Channel Response Function

The channel response function is traditionally used to characterize the input–output relationship of a transmission medium. The time or frequency response of the output for any given input can be obtained from the channel response function. In the following, the relationship between the direct LOS signal and the scattered signal is modeled in terms of a channel response function. This argument is justifiable as the scattered signals undergo additional path delay, fading, and environmental effect in comparison with the direct LOS signals. One can thus use the channel response function to model the gain, phase, polarization, and delay characteristics of the additional scattering phenomena. Let $y_{\text{direct}}$ and $y_{\text{reflected}}$ be the received signal waveforms along the direct LOS and reflected paths, respectively. As discussed in the previous section, these two waveforms bear squared autocorrelation function shapes. Fig. 6 depicts the role of the channel response function and its relationship with the scattering phenomena. The waveform $y_{\text{direct}}$ depends on the LOS dynamics and the receiver dynamics. The former is attributed to spreading loss, atmospheric effects, and so forth. The latter, in contrast, is governed by the antenna gain, RFFE, and correlation processing. In contrast, $y_{\text{reflected}}$ is affected by the more complicated scattering phenomena. The channel

response function is identified by using $y_{\text{direct}}$ and $y_{\text{reflected}}$ in the modeling process. This typically results in a function that is subject to gain, delay, and phase variations. As the direct LOS dynamics are well understood, one can thus use to channel response function to deduce the reflection dynamics and reveal remote sensing variables. It is clear that the channel response function is not sensitive to the variation of the transmitted power of the GNSS satellite.

Suppose that the dynamics are linear; then, the channel response function $h(\tau)$ relates $y_{\text{direct}}$ to $y_{\text{reflected}}$ through

$$y_{\text{reflected}}(\tau) = h(\tau) \star y_{\text{direct}}(\tau) \tag{10}$$

where the symbol $\star$ denotes the convolution operation. In the Laplace $s$ domain, the channel response function is represented in terms of a transfer function as follows:

$$H(s) = \frac{n(s)}{d(s)}\, e^{-\gamma s} \tag{11}$$

where $n(s)$ and $d(s)$ are polynomials of $s$, and $\gamma$ is the time delay. The time delay can often be estimated through the difference: the path delay from the GNSS satellite to the specular reflection point and to the GNSS-R receiver in comparison with the path delay from the GNSS satellite to the GNSS-R receiver along the direct LOS path. The factor $\frac{n(s)}{d(s)}$ is used to characterize the gain and phase variations between the direct LOS and scattered signals. A simplest form of (11) is a first-order model as follows:

$$H(s) = \frac{b}{s+a}\, e^{-\gamma s}. \tag{12}$$

In the above model, the parameter $a$ governs the bandwidth of the system and can be related to the roughness and effective area of the reflection surface. Both $a$ and $b$ are related to the gain of the system, which depends on the reflection surface properties. Naturally, in building the model, the antenna gains and RFFE gains in the direct signal path and reflection signal path need to be taken into account. The corresponding impulse response function in the time domain of (12) is given by

$$h(\tau) = b\, e^{-a(\tau-\gamma)}. \tag{13}$$

The channel response function accepts the squared autocorrelation function as input and render the delay waveform of scattered signal as the output. To see the effectiveness of the simple model (12), it is assumed that the input is the squared autocorrelation function $\Lambda^2_{\text{BPSK}}(\tau)$ with $\eta = 2$, and the resulting output waveforms after normalization and shifting under different $a$ are shown in Fig. 7. Note that the well-known flattening effect, as described in [10] and [25], is clearly observed. Thus, the simple model in (12) or (13) can be used to characterize the relationship between the direct LOS BPSK waveform and the reflected BPSK waveform. Suppose that the input is the filtered squared autocorrelation function $\Lambda^2_{\text{BOC}}(\tau)$; the output waveforms under different $a$ are depicted in Fig. 8. The waveforms bear a similar form of reflected Galileo signal as reported in [36].

### B. Synergy of BPSK and BOC Signals

To see that the channel response function is equally applicable to BPSK and BOC-modulated signals, consider the following four waveforms: direct LOS BPSK-modulated signal ($y_{\text{direct,BPSK}}$), direct LOS BOC-modulated signal ($y_{\text{direct,BOC}}$), reflected BPSK-modulated signal ($y_{\text{reflected,BPSK}}$), and reflected BOC-modulated signal ($y_{\text{reflected,BOC}}$). Fig. 9 depicts the relationship among the aforementioned four signal components. For each signal component, the squaring block represents the noncoherent accumulation operation. Let $\Lambda_{\text{BPSK}}(\tau)$ and

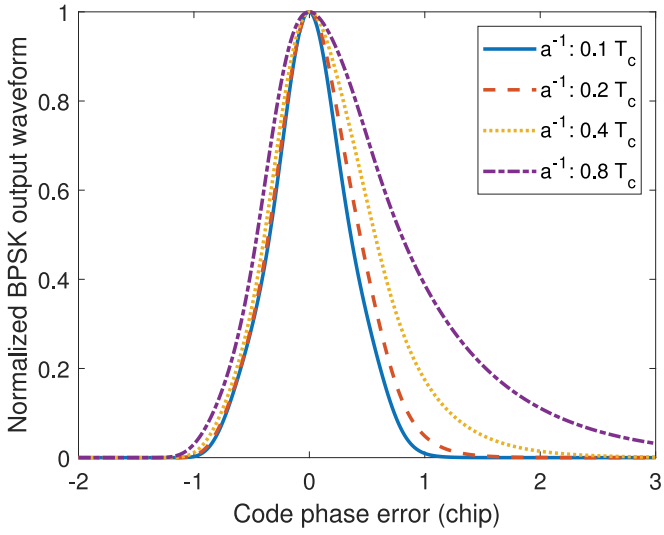


Fig. 7. BPSK output waveforms under different $a$.

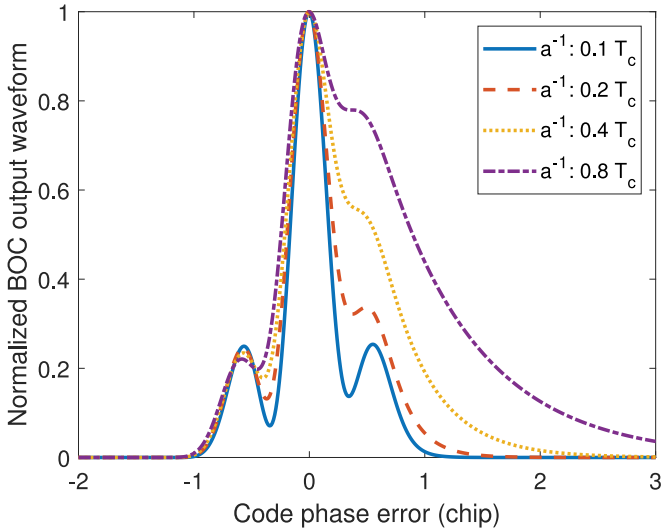


Fig. 8. BOC output waveforms under different $a$.

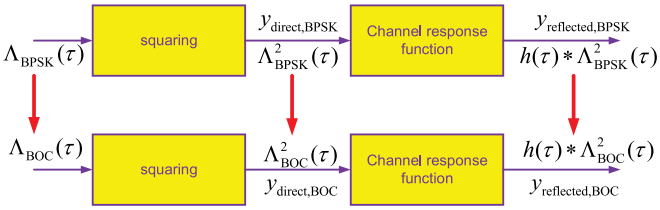


Fig. 9. Relationship among direct LOS and scattered BPSK and BOC signals.

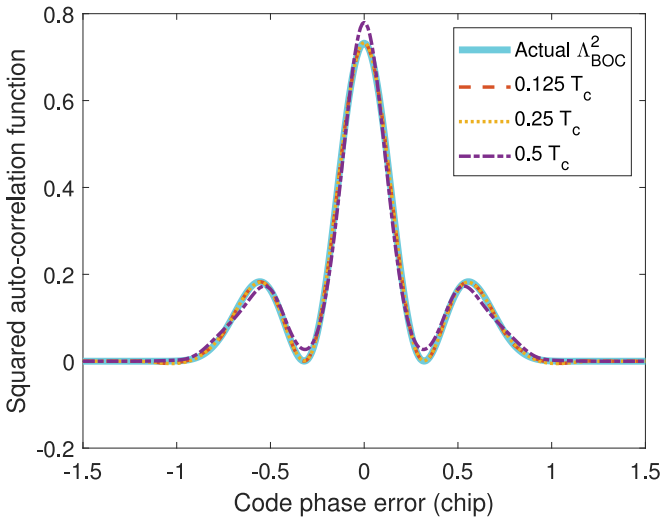


Fig. 10. Function $\Lambda^2_{\mathrm{BOC}}$ and its approximations under different grid resolutions.

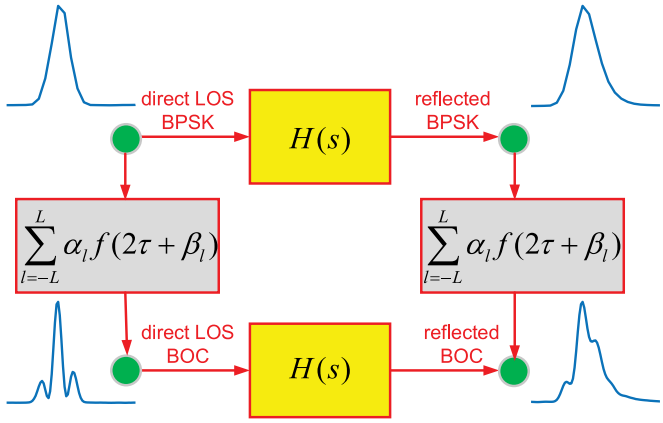


Fig. 11. Commutative diagram is relating signals of interest.

$\Lambda_{\mathrm{BOC}}(\tau)$ be the autocorrelation functions of BPSK- and BOC-modulated signals, respectively. The delay waveforms of the direct LOS signals, i.e., $y_{\mathrm{direct,BPSK}}$ and $y_{\mathrm{direct,BOC}}$, resemble $\Lambda^2_{\mathrm{BPSK}}(\tau)$ and $\Lambda^2_{\mathrm{BOC}}(\tau)$, respectively. The channel impulse response function is assumed to be $h(\tau)$, and the output is denoted as the convolution of the input and the channel response function.

The shapes of $\Lambda_{\mathrm{BPSK}}(\tau)$ and $\Lambda_{\mathrm{BOC}}(\tau)$ are illustrated in Fig. 4. It is noted that in the case that the front end bandwidth is infinite, the two autocorrelation functions are analytically related. Indeed, $\Lambda_{\mathrm{BOC}}(\tau)$ can be expressed as a combination of scaled, shifted, and dilated versions of $\Lambda_{\mathrm{BPSK}}(\tau)$ as follows:

$$\Lambda_{\mathrm{BOC}}(\tau) = -\frac{1}{2}\Lambda_{\mathrm{BPSK}}(2\tau+1) + \Lambda_{\mathrm{BPSK}}(2\tau) - \frac{1}{2}\Lambda_{\mathrm{BPSK}}(2\tau-1). \tag{14}$$

In GNSS-R, the squared autocorrelation function is of interest as squaring operation and noncoherent accumulation are involved. The squared autocorrelation function $\Lambda^2_{\mathrm{BOC}}(\tau)$ cannot be expressed as an analytic function of $\Lambda^2_{\mathrm{BPSK}}(\tau)$. However, an approximation can be made as follows:

$$\Lambda^2_{\mathrm{BOC}}(\tau) \approx \sum_{l=-L}^{L} \alpha_l \, \Lambda^2_{\mathrm{BPSK}}(2\tau+\beta_l) \tag{15}$$

for some $\alpha_l$ and $\beta_l$. Note that both $\Lambda^2_{\mathrm{BPSK}}(\tau)$ and $\Lambda^2_{\mathrm{BOC}}(\tau)$ are locally supported; the number of coefficients which is governed by $L$ in (15) is finite. A uniform grid of $\beta_l$ is adopted, and the closeness of the approximation depends on the resolution of $\beta_l$ since the coefficients $\alpha_l$ can be determined by a least squares method. It is further observed that as the functions are symmetric, the coefficients satisfy $\alpha_l = \alpha_{-l}$ when $\beta_l = -\beta_l$. Fig. 10 depicts the function $\Lambda^2_{\mathrm{BOC}}$ and its approximations under different resolutions with the $\alpha_l$ optimally determined and the bandwidth factor $\eta = 2$. As an example, when the resolution is $0.25T_c$, the $\beta_l$ are $-1.5T_c$, $-1.25T_c, \ldots, 1.25T_c$, $1.5T_c$. From Fig. 10, if the resolution is $0.5T_c$, then an error is observed at zero code phase. However, the function $\Lambda^2_{\mathrm{BOC}}(\tau)$ can be closely approximated in terms of a set of $\Lambda^2_{\mathrm{BPSK}}(2\tau+\beta_l)$ with a resolution $0.25T_c$ or smaller.

Under the assumption that the system is linear, the approximation in (15) implies that

$$\begin{aligned} & h(\tau) \star \Lambda^2_{\mathrm{BOC}}(\tau) \\ & \approx h(\tau) \star \left( \sum_{l=-L}^{L} \alpha_l \, \Lambda^2_{\mathrm{BPSK}}(2\tau+\beta_l) \right) \\ & \approx \sum_{l=-L}^{L} \alpha_l \, \left( h(\tau) \star \Lambda^2_{\mathrm{BPSK}}(2\tau+\beta_l) \right). \end{aligned} \tag{16}$$

The above relationship reveals that it is possible to deduce the delay waveform of scattered BOC-modulated signals based on delay waveforms of scattered BPSK-modulated signals. Moreover, one can utilize the above relationship to perform quality verification and remote sensing data retrieval. More importantly, the channel response function can be applicable to both BPSK- and BOC-modulated signals.

In the channel response function modeling approach, the effect of scattering is considered from a system input–output perspective. The effect of scattering may result in a delay waveform that is a composition of a set of distributed, delayed, attenuated, and distorted copies of the original profile. With the channel response function in hand, a commutative diagram in Fig. 11 can be established. The implications of this analysis framework are multifold.

1) The dependence of transmitter power is primarily removed as the transfer function $H(s)$ accounts for the relative power between the direct LOS signal and the scattered signal. It is expected that the data retrieval based on the model is more robust.
2) The channel response function can be appropriately adjusted to model the input–output behavior by adjusting the order and parameters. System identification toolboxes exist and can be brought to bear.

3) Both BPSK- and BOC-modulated signals are utilized in the data processing. Through the approximation, these two signals can be simultaneously assessed for signal quality verification and for an enhanced data product.

This framework is expected to pave the way for a model-based data retrieval approach. Existing GNSS-R data retrieval approaches are signal-based, in which a forward scattering model from $u$ to $y_{\text{reflected}}$ as highlighted in the shaded yellow curve in Fig. 6 is adopted. Through a careful calibration of receiver gain, RFFE, and signal processing parameters together with information on the input $u$, the parameters associated with the reflection dynamics are retrieved through bistatic radar cross section and geophysical model function [37]. The model-based approach differs from the signal-based approach as the model between $y_{\text{reflected}}$ and $y_{\text{direct}}$ is identified and used in the GNSS-R remote sensing. To completely develop the model-based GNSS-R remote sensing application, the forward model as depicted in terms of red-dashed lines in Fig. 6 is currently under development through extensive simulations. In TRITON GNSS-R remote sensing, the observed $y_{\text{direct}}$ and $y_{\text{reflectd}}$ will be processed to obtain coefficients of the channel response function. The remote sensing parameters such as ocean wind speed are then retrieved from the coefficients and the forward model. A limitation of the proposed model-based approach is that two signal processing chains need to be calibrated. This additional task, however, is considered manageable. Indeed, some parameters along these two signal processing chains are common and can indeed simplify the task. It is anticipated with the deployment of the TRITON mission that sufficient amount of data can be collected to tune this model of data retrieval. In this aspect, the commutative diagram serves as a means for the data quality check and receiver calibration as redundant data are available and can be processed under this framework. To this end, it is important to verify that the channel response function of the BPSK-modulated signal is applicable to the BOC-modulated signal. This verification is discussed in the next section through an airborne test and data analysis.

## V. Flight Test and Data Analysis

In this section, the flight test of the TRITON GNSS-R receiver is described and the data are analyzed. The GNSS-R receiver has indeed been tested in a series of airborne tests to verify its functionalities, assess the data qualities, and check the data processing software. In a flight test conducted in 2016, the GNSS-R receiver is installed in AIDC (Aerospace Industrial Development Corporation, Taiwan) aircraft to test the real-time DDM generation and data archiving capabilities. Fig. 12 depicts the flight path and the sky plot at one instant. The aircraft took off at Taichung CCK airport, flew over Penghu islands, and back to CCK. The sky plot illustrates that there are several GNSS satellites that can be utilized for reflectometry. As the purpose is to compare and synergize BPSK- and BOC-modulated signals, three signals, which are originated from GPS pseudorandom number (PRN) 17, Galileo PRN 14, and QZSS PRN193 satellites, respectively, are marked for further discussions in the following. Note that the elevations of these three satellites are close. All these satellites

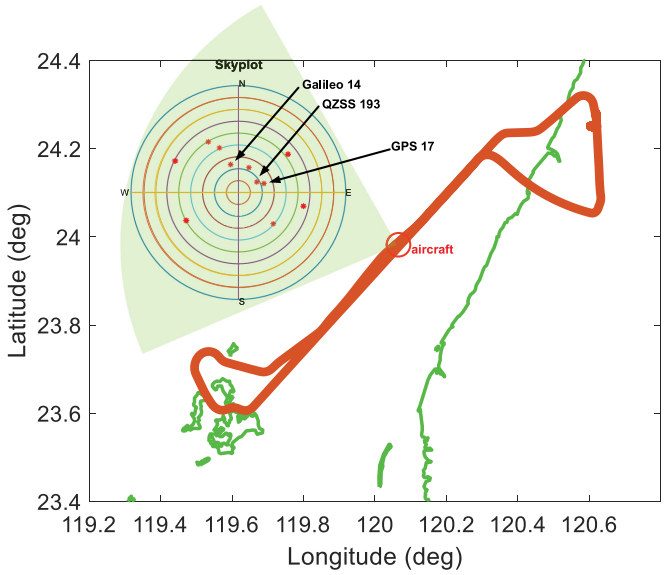


Fig. 12. Flight path and sky plot.

broadcast navigation signals in the L1 band, and the GNSS-R receiver is able to receive the direct LOS and reflected signals from these satellites. The signal from the GPS satellite is the legacy L1 C/A signal, in which the BPSK modulation is used. In contrast, the signal from the Galileo satellite is under BOC modulation. The signals from the QZSS satellite are unique in the sense that there are two L1 C/A BPSK-modulated signal components and one L1C BOC-modulated signal component that can be observed. Table I lists the signal components and the associated parameters.

### A. Delay Waveforms of BPSK- and BOC-Modulated Signals

The DDM of a GPS signal is obtained by correlating the incoming signal with a set of local replica at different code phases and Doppler frequencies. The delay waveform is obtained from the DDM at the central Doppler frequency. The normalized delay waveforms with respect to the direct LOS signal and the reflected signal of GPS PRN 17 satellite are depicted in Fig. 13. The horizontal axes of the two waveforms are adjusted so that the two waveforms are aligned and can be more easily compared. It is noted that the former exhibits a shape that resembles the square of a triangle function. In contrast, the delay waveform with respect to the reflected signal has a noticeable trailing edge due to the contributions from scattered signals at longer propagation paths.

The direct LOS and reflected signals with respect to the Galileo PRN 14 satellite are also processed, resulting in the delay waveforms in Fig. 14. It is noted that the delay waveforms are subject to one main peak and two sidelobes. For the direct LOS signals, the power of the two sidelobes is about the same, which is one-quarter of that of the main lobe. The situation is different in the scattered signal: the sidelobe at the leading edge remains similar, while the sidelobe at the trailing edge is distorted due

TABLE I
L1 BAND SIGNAL COMPONENTS OF GPS, GALILEO, AND QZSS

| System | signal component | | Chipping rate | Code length | Overlay code | Modulation |
|---|---|---|---|---|---|---|
| GPS/QZSS | L1 C/A | | 1.023 Mcps | 1023 chips | - | BPSK |
| GPS/QZSS | L1C | L1CD | 1.023 Mcps | 10230 chips | - | BOC |
| | | L1CP | 1.023 Mcps | 10230 chips | L1CO | BOC, TMBOC |
| Galileo | E1 | | 1.023 Mcps | 4092 chips | - | CBOC |
| QZSS | L1S | | 1.023 Mcps | 1023 chips | - | BPSK |

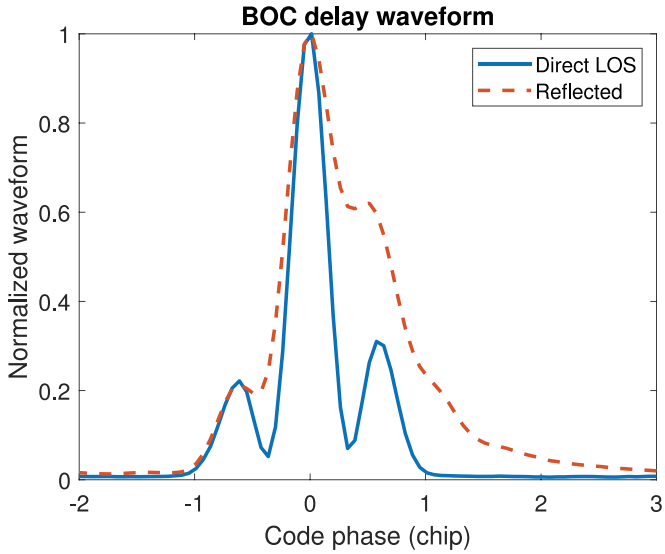


Fig. 13. Delay waveforms for direct LOS and reflected BPSK-modulated signals.

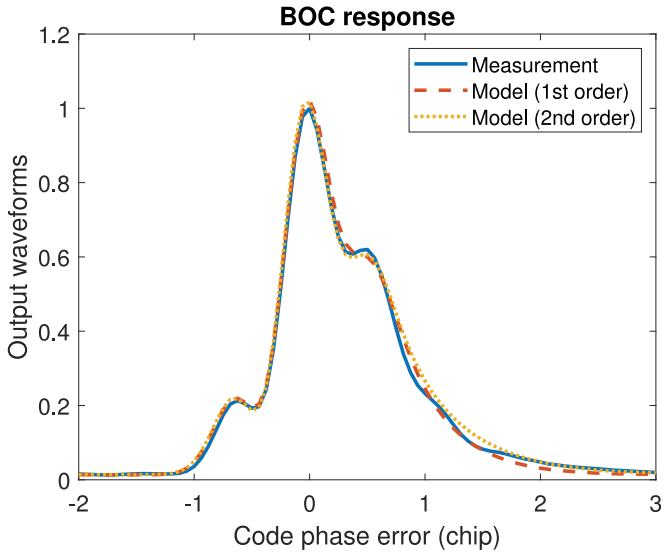


Fig. 15. Comparison of the measured and modeled delay BPSK waveforms.

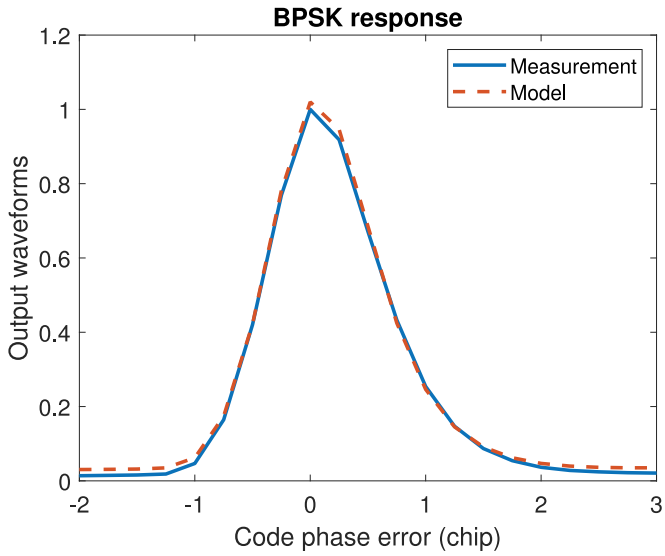


Fig. 14. Delay waveforms for direct LOS and reflected BOC-modulated signals.

to the accumulations from some delayed and attenuated signal components.

The delay waveforms of BPSK and BOC signals possess distinct features. Both waveforms are not symmetric to the center, and the trailing edge tends to be flatten. Yet, the BOC-reflected waveform is more noticeable for the two sidelobes. The peak of the sidelobe at the leading edge remains similar in magnitude in comparison with the ideal waveform. In contrast, the peak of the trailing edge sidelobe is enhanced. Thus, in comparison with the BPSK-reflected waveform, the BOC-reflected waveform appears to be richer in contents. For example, one can compare the two peaks of the sidelobes to obtain asymmetric data for information retrieval. On the other hand, it is also pointed out that a higher resolution in processing BOC-reflected waveform is needed so that the fine details can be observed and processed. Currently, the GNSS-R retrieval algorithms may use peak value, leading edge slope, and waveform parameters to deduce information of the reflecting surface. Based on the above analysis, it is clear that the existing algorithms for BPSK-reflected signal retrieval need to be appropriately revised when processing BOC-reflected signals.

The channel response function discussed previously may serve as a means in data retrieval as it is applicable to both BPSK- and BOC-modulated signals. To see the feasibility, the direct LOS waveform and the reflected waveform in Fig. 13 are regarded as the input and the output of the system, respectively. A first-order model as in (12) is established to render the parameters of the model by matching the input and output response. This results in a model with coefficient $a = 2.54$. Based on the first-order model, the predicted output is evaluated by using the same input. Fig. 15 depicts the waveforms from measurement and model. It is noted that the predicted waveform

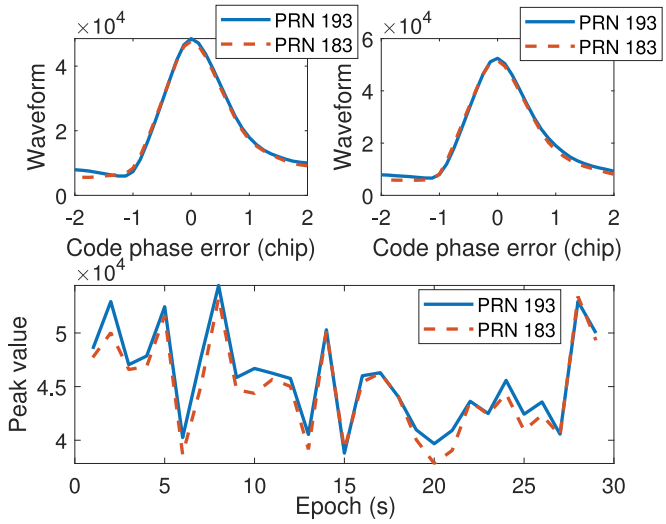


Fig. 16. Comparison of the measured and modeled delay BOC waveforms.

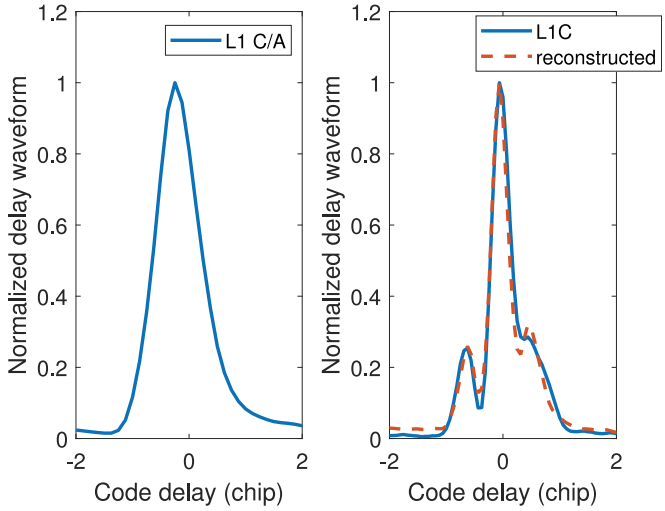


Fig. 17. QZSS 193 and 183 delay waveforms and peak values.

from the model matches the measured waveform reasonably well. Thus, the model can be used to reflect the dynamic of the reflection phenomena. A similar task is performed for the BOC signals, and the corresponding coefficient of the first-order model is $a = 2.56$, which is sufficiently close to that of the BPSK signal model. The results are illustrated in Fig. 16, which again demonstrate the effectiveness of the channel response function approach. In Fig. 16, the result of a second-order model match is also provided. From the flight data analyses, it is verified that the channel response function can be used to characterize the relationship between the direct LOS waveform and the scattered waveform. Furthermore, the same model is equally applicable to BPSK- and BOC-modulated signals.

### *B. QZSS Signal Processing*

In modernized GNSS, the satellites transmit the ranging signal with different spreading codes and modulations at the same frequency. For example, in GPS III, the L1 C/A and L1C signal components are transmitted at the same frequency band. From the perspective of GNSS-R, the two signal components essentially arrive at the receiver along the same propagation path. Therefore, if the receiver is able to receive and process the two signal components, some additional benefits can be obtained. For a receiver operating in the L1 band to receive the QZSS signal, the C/A, L1C, and L1S components can processed. The former two are used for PNT service, while the latter is for submeter-level augmentation service (see [38] and [39] for details). Table I lists some important parameters for the purpose of comparison. The L1 C/A signal component is the legacy signal component. For the QZSS satellite, the L1S signal component utilizes a spreading code that is similar to a C/A code with a different PRN. For example, for the QZS-1 satellite, its PRN for L1 C/A navigation service is 193 and the PRN for L1S augmentation service is 183. The QZS-1 satellite also broadcasts L1C signals, which can be used for PNT and reflectometry applications. In the airborne experiment, QZS-1 satellite signals are received and processed. In the following, two results are discussed. The first result is for the airborne GNSS-R receiver to receive two signals under the same modulation and similar path. The result essentially reveals the sensitivity of absolute-power-based data retrieval, and that the channel response model that relies on the relative power may have advantages. The second result investigates the scattered L1 C/A and L1C signals along the same reflection path and verifies the commutative diagram.

In the airborne experiment, the receiver processes the PRN 193 and PRN 183 signals from the same QZS-1 satellite along the same path. These two signals are under BPSK modulation with different spreading codes. The top two plates in Fig. 17 are delay waveforms of the two scattered signal components at different epochs. Note that the two profiles are sufficiently close. Yet, it is observed that at different epochs, even though the reflection geometry and surface properties are expected to be similar in the observation period (30 s), the peak values are different epoch by epoch. This is illustrated in the bottom plate of the figure, in which the peak power values of the PRN 193 reflected signal vary between $3.88 \times 10^4$ and $5.44 \times 10^4$ (in count) with a standard deviation $4.35 \times 10^3$. The variation affects the data retrieval result. It is observed that the peak values of PRN 193 and PRN183 signals are highly correlated. Thus, a channel response model appears to be a better option in dealing with peak power variation, which may be resulted from navigation data bit transition, transmitter power, and others.

The GNSS-R receiver processes the BPSK-modulated L1 C/A and BOC-modulated L1C signals from the same QZSS satellite along both the LOS and reflected paths. In view of Fig. 11, the four delay waveforms are thus available. The waveform of the direct LOS BOC-modulated signal is related to the waveform of the direct LOS BPSK-modulated signal through (15). In this approximation, the grid resolution is set as $0.25T_c$, and the coefficients $\alpha_l$ are determined by using a least squares method. Table II depicts the coefficients. With this model and coefficients, one could then predict the waveform of the reflected

TABLE II
COEFFICIENTS IN APPROXIMATION

| $l$ | 0 | 1 | 2 | 3 | 4 | 5 | 6 |
|---|---|---|---|---|---|---|---|
| $\alpha_l$ | 1.3047 | −0.1924 | −0.1698 | −0.1544 | 0.4084 | −0.0426 | −0.0029 |
| $\beta_l$ in $T_c$ | 0 | 0.25 | 0.50 | 0.75 | 1.00 | 1.25 | 1.50 |

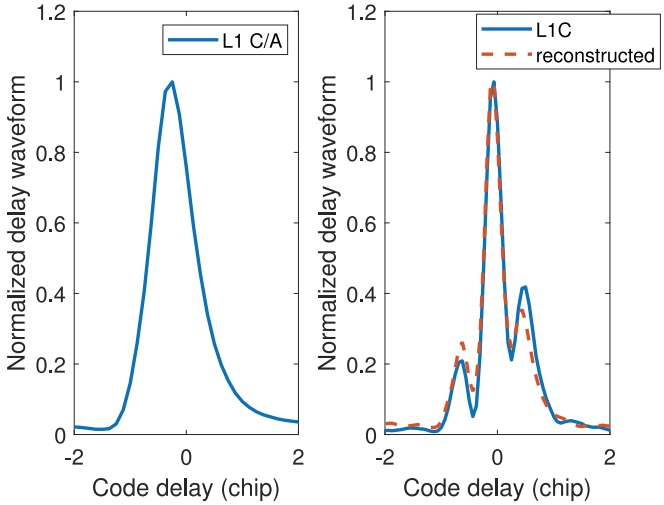


Fig. 18. QZSS scattered signals in L1 C/A, L1C, and the reconstructed result at one instant.

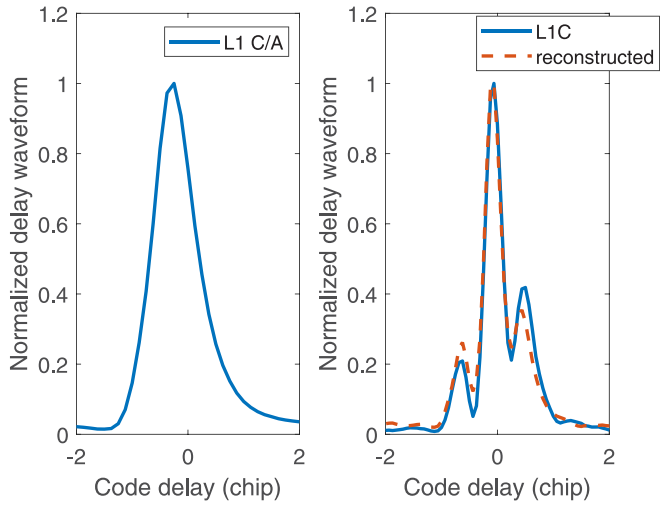


Fig. 19. QZSS scattered signals in L1 C/A, L1C, and the reconstructed result at another instant.

BOC-modulated signal given the waveform of the reflected BPSK-modulated signal. Figs. 18 and 19 depict two results at different epochs. The left plates in the figures are normalized delay waveforms of the scattered L1 C/A signals, and the right plates show that delay waveforms of the scattered L1C signals and the reconstructed waveforms based on L1 C/A signals and the model. The closeness of the measured waveform and the reconstructed waveform verifies the commutative diagram in Fig. 11. Consequently, the potential advantages as mentioned at the end of the previous section in remote sensing can and will be explored.

## VI. CONCLUSION

The article describes the upcoming TRITON GNSS-R mission for the remote sensing of ocean wind speed. In this envisioned mission, the GNSS-R receiver can receive both BPSK- and BOC-modulated signals along the direct LOS and scattered paths. To exploit this opportunity, the channel response function is proposed to model the scattering phenomena by relating the direct LOS signal waveform to the scattered signal waveform. This model can be used to characterize the relative gain, phase, and delay between the two propagation paths and, as a result, is less prone to the variation of the transmitter power. By processing BPSK- and BOC-modulated signals and by observing that the squared autocorrelation functions can indeed be related, a GNSS-R signal analysis framework or commutative diagram is proposed for the verification of signal quality and calibration of the GNSS-R processing. Results of the TRITON GNSS-R receiver in a flight test are provided to verify the feasibility and effectiveness of the channel response function and commutative diagram.

In the future, a calibration procedure based on the commutative diagram will be further developed, and the channel response function will be extended to account for the relationship between DDMs of the direct LOS and scattered signals. Moreover, the data retrieval method that is based on the channel response model will be investigated.

## REFERENCES

[1] GPS website. [Online]. Available: http://www.gps.gov/, Accessed on: Nov. 1, 2019.
[2] GLONASS website, 2020. [Online]. Available: https://www.glonass-iac.ru/en, Accessed on: Nov. 1, 2019.
[3] Galileo service center website, 2020. [Online]. Available: https://www.gsc-europa.eu, Accessed on: Nov. 1, 2019.
[4] BDS website, 2020. [Online]. Available: https://www.beidou.gov.cn, Accessed on: Nov. 1, 2019.
[5] QZSS website, 2020. [Online]. Available: https://www.qzss.go.jp, Accessed on: Nov. 1, 2019.
[6] J. Awange, *GNSS Environmental Sensing*, 2nd ed. Berlin, Germany: Springer, 2018.
[7] S. Jin, E. Cardellach, and F. Xie, *GNSS Remote Sensing: Theory, Methods, and Applications*. Berlin, Germany: Springer-Verlag, 2014.
[8] V. U. Zavorotny, S. Gleason, E. Cardellach, and A. Camps, "Tutorial on remote sensing using GNSS bistatic radar of opportunity," *IEEE Geosci. Remote Sens. Mag.*, vol. 2, no. 4, pp. 8–45, Dec. 2014.
[9] M. Martin-Neira, "A passive reflectometry and interferometry system (PARIS)—Application to ocean altimetry," *ESA J.*, vol. 17, no. 4, pp. 331–355, 1993.
[10] J. L. Garrison, A. Komjathy, V. U. Zavorotny, and S. J. Katzberg, "Wind speed measurement from forward scattered GPS signals," *IEEE Trans. Geosci. Remote Sens.*, vol. 40, no. 1, pp. 50–65, Jan. 2002.
[11] V. U. Zavorotny and A. G. Voronovich, "Scattering of GPS signals from the ocean with wind remote sensing application," *IEEE Trans. Geosci. Remote Sens.*, vol. 38, no. 2, pp. 951–964, Mar. 2000.
[12] S. T. Lowe, J. L. LaBrecque, C. Zuffada, L. J. Romans, L. E. Young, and G. A. Hajj, "First spaceborne observation of an Earth-reflected GPS signal," *Radio Sci.*, vol. 37, no. 1, pp. 1–28, Jan. 2002.

[13] S. Gleason, "Remote sensing of ocean, ice and land surfaces using bistatically scattered GNSS signals from low earth orbit," Ph.D. dissertation, Appl. Physics, Univ. Surrey, Guildford, U.K., 2006.
[14] M. P. Clarizia, C. Gommenginger, S. Gleason, C. Galdi, and M. Unwin, "Global navigation satellite system-reflectometry (GNSS-R) from the UK-DMC satellite for remote sensing of the ocean surface," in *Proc. IEEE Int. Geosci. Remote Sens. Symp.*, 2008.
[15] A. da Silva Curiel, D. Liddle, V. O'Donovan, M. Unwin, and M. Sweeting, "First results from the UK TechDemoSat-1 spacecraft," in *Proc. 10th IAA Symp. Small Satell. Earth Observ.*, 2015, pp. I-276–I-279.
[16] M. Unwin, "Towards a GNSS reflectometry service for UK TDS-1 satellite," in *Proc. IEEE GNSS+R Workshop*, 2019.
[17] C. Ruf, S. Gleason, D. McKague, M. Moghaddam, and D. Posselt, "NASA CYGNSS science data characterization and applications," in *Proc. IEEE GNSS+R Workshop*, 2019.
[18] C. Ruf and R. Balasubramaniam, "Development of CYGNSS geophysical model function for wind speed," *IEEE J. Sel. Topics Appl. Earth Oberv. Remote Sens.*, vol. 12, no. 1, pp. 66–77, Jan. 2019.
[19] M. Unwin, P. Jales, P. Blunt, S. Duncan, M. Brummitt, and C. Ruf, "The SGR-ReSI and its application for GNSS reflectometry on the NASA EV-2 CYGNSS mission," in *Proc. IEEE Aerosp. Conf.*, 2013, pp. 1–6.
[20] J. C. Juang, S. H. Ma, and C. T. Lin, "Study of GNSS-R techniques for FORMOSAT mission," *IEEE J. Sel. Topics Appl. Earth Observ. Remote Sens.*, vol. 9, no. 10, pp. 4582–4592, Oct. 2016.
[21] J. C. Juang, Y. F. Tsai, and C. T. Lin, "FORMOSAT-7R mission for GNSS reflectometry," in *Proc. IEEE Int. Geosci. Remote Sens. Symp.*, 2019, pp. 5177–5180.
[22] J. W. Betz, *Engineering Satellite-Based Navigation and Timing: Global Navigation Satellite Systems, Signals, and Receivers*. Hoboken, NJ, USA: Wiley-IEEE Press, 2015.
[23] E. D. Kaplan and C. J. Hegarty, Eds, *Understand GPS/GNSS Principles and Applications*, 3rd ed. Norwood, MA, USA: Artech House, 2017.
[24] P. J. G. Teunissen and O. Montenbruck, editors, *Handbook of Global Navigation Satellite Systems*, Berlin, Germany: Springer, 2017.
[25] D. Pascual, H. Park, A. Camps, A. Alonso, and R. Onrubia, "Comparison of GPS L1 and Galileo E1 signals for GNSS-R ocean altimetry," in *Proc. IEEE Int. Geosci. Remote Sens. Symp.*, 2013, pp. 358–361.
[26] A. G. Voronovich and V. U. Zavorotny, "Bistatic radar equation for signals of opportunity revisited," *IEEE Trans. Geosci. Remote Sens.*, vol. 56, no. 4, pp. 1959–1968, Apr. 2018.
[27] S. Gleason, C. S. Ruf, A. J. O'Brien, and D. S. McKague, "The CYGNSS level 1 calibration algorithm and error analysis based on on-orbit measurements," *IEEE J. Sel. Topics Appl. Earth Observ. Remote Sens.*, vol. 12, no. 1, pp. 37–49, Jan. 2019.
[28] F. Said, Z. Jelenak, P. S. Chang, and S. Soisuvarn, "An assessment of CYGNSS normalized bistatic radar cross section calibration," *IEEE J. Sel. Topics Appl. Earth Observ. Remote Sens.*, vol. 12, no. 1, pp. 50–65, Jan. 2019.
[29] D. S. McKague and C. S. Ruf, "CYGNSS constellation intercalibration," in *Proc. IEEE Int. Geosci. Remote Sens. Symp.*, 2017.
[30] National Space Organization, Taiwan. [Online]. Available: http://www.nspo.narl.org.tw/, Accessed on: Nov. 1, 2019.
[31] C. Zuffada, T. Elfouhaily, and S. Lowe, "Sensitivity analysis of wind vector measurements from ocean reflected GPS signals," *Remote Sens. Environ.*, vol. 88, no. 3, pp. 341–350, 2003.
[32] D. M. Lin and J. B. Y. Tsui, "Comparison of acquisition methods for software GPS receiver," in *Proc. Int. Tech. Meeting Satellite Division Inst. Navig.*, 2000, pp. 2385–2390.
[33] C. Yang, "Zoom, pruning, and partial FFT for GPS signal tracking," in *Proc. Nat. Tech. Meeting Inst. Navigat.*, 2001, pp. 839–849.
[34] Surrey Satellite Technology Limited, "MERRByS product manual-GNSS reflectometry on TDS-1 with the SGR-ReSI," 2018. [Online]. Available: http://www.merrbys.co.uk/
[35] H. Park, D. Pascual, A. Camps, F. Martin, A. Alonso-Arroyo, and H. Carreno-Luengo, "Analysis of spaceborne GNSS-R delay-doppler tracking," *IEEE J. Sel. Topics Appl. Earth Observ. Remote Sens.*, vol. 7, no. 5, pp. 1481–1492, May 2014.
[36] J. C. Juang, "Data analysis of Galileo reflected signals in an airborne experiment," in *Proc. IEEE GNSS+R Workshop*, 2017.
[37] C. Ruf *et al. CYGNSS Handbook*. Ann Arbor, MI, USA: Michigan Publishing, 2016.
[38] Cabinet Office (Japan) and Quasi-Zenith Satellite System Navigation Service, "QZSS interface specification: Satellite positioning, navigation, and timing service," 2018. [Online]. Available: https://qzss.go.jp/en/technical/ps-is-qzss/ps-is-qzss.html
[39] Cabinet Office (Japan) and Quasi-Zenith Satellite System Navigation Service, "QZSS interface specification: Sub-meter level augmentation service," 2018. [Online]. Available: https://qzss.go.jp/en/technical/ps-is-qzss/ps-is-qzss.html

**Jyh-Ching Juang** (Member, IEEE) received the B.S. degree in control engineering and M.S. degree in electronics from National Chiao-Tung University, Hsinchu, Taiwan, in 1980 and 1982, respectively, and the Ph.D. degree in electrical engineering from the University of Southern California, Los Angeles, CA, USA, in 1987.

He was with Lockheed Martin Aeronautics Company, Burbank, CA, before he joined the Faculty of the Department of Electrical Engineering, National Cheng Kung University, Tainan, Taiwan, in 1993, where he is currently a Professor. His research interests include robust control, global navigation satellite system (GNSS) signal processing, GNSS reflectometry, and autonomous driving.

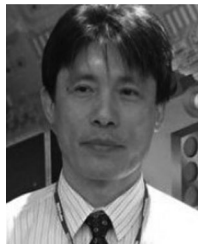

**Chen-Tsung Lin** received the B.S. degree in electrical engineering from National Taiwan Science and Technology University, Taipei, Taiwan, in 1988, and the M.S. degree in control engineering from National Chiao-Tung University, Hsinchu, Taiwan, in 1994.

He worked for Acer Computer Incorporated, Taipei, for six years before he joined National Space Organization (NSPO), Hsinchu, Taiwan, where he is currently a Program Manager of the Triton Satellite Program. He has been with NSPO for 20 years. His research interests include development of spacecraft attitude control systems and spacecraft attitude control components.

**Yung-Fu Tsai** received the B.S. degree from National Tsing Hua University, Hsinchu, Taiwan, in 2003, and the M.S. and Ph.D. degrees from National Cheng Kung University, Tainan, Taiwan, in 2005 and 2009, respectively.

He is currently an Associate Researcher with National Space Organization, Hsinchu. His research interests include global positioning system/global navigation satellite system navigation processing algorithm and micro/nano experimental satellites.